**Luca De Vincentiis**[1]
Department of Mechanics,
Linné FLOW Centre,
KTH Royal Institute of Technology,
Osquars backe 18,
114 28, Stockholm, Sweden
e-mail: ldv@mech.kth.se

**Kristina Đurović**
Department of Mechanics,
Linné FLOW Centre,
KTH Royal Institute of Technology,
Osquars backe 18,
114 28, Stockholm, Sweden

**Davide Lengani**
DIME-University of Genova,
via alla Opera Pia 15,
16145, Genova, Italy

**Daniele Simoni**
DIME-University of Genova,
via alla Opera Pia 15,
16145, Genova, Italy

**Jan Pralits**
DICCA-University of Genova,
viale Cambiaso, 6,
16145, Genova, Italy

**Dan S. Henningson**
Department of Mechanics,
Linné FLOW Centre,
KTH Royal Institute of Technology,
Osquars backe 18,
114 28, Stockholm, Sweden

**Ardeshir Hanifi**
Department of Mechanics,
Linné FLOW Centre,
KTH Royal Institute of Technology,
Osquars backe 18,
114 28, Stockholm, Sweden

# Effects of Upstream Wakes on the Boundary Layer Over a Low-Pressure Turbine Blade

*In the present work, the evolution of the boundary layer over a low-pressure turbine blade is studied using direct numerical simulations, with the aim of investigating the unsteady flow field induced by the rotor-stator interaction. The freestream flow is characterized by the high level of freestream turbulence and periodically impinging wakes. As in the experiments, the wakes are shed by moving bars modeling the rotor blades and placed upstream of the turbine blades. To include the presence of the wake without employing an ad-hoc model, we simulate both the moving bars and the stationary blades in their respective frames of reference and the coupling of the two domains is done through appropriate boundary conditions. The presence of the wake mainly affects the development of the boundary layer on the suction side of the blade. In particular, the flow separation in the rear part of the blade is suppressed. Moreover, the presence of the wake introduces alternating regions in the streamwise direction of high- and low-velocity fluctuations inside the boundary layer. These fluctuations are responsible for significant variations of the shear stress. The analysis of the velocity fields allows the characterization of the streaky structures forced in the boundary layer by turbulence carried by upstream wakes. The breakdown events are observed once positive streamwise velocity fluctuations reach the end of the blade. Both the fluctuations induced by the migration of the wake in the blade passage and the presence of the streaks contribute to high values of the disturbance velocity inside the boundary layer with respect to a steady inflow case. The amplification of the boundary layer disturbances associated with different spanwise wavenumbers has been computed. It was found that the migration of the wake in the blade passage stands for the most part of the perturbations with zero spanwise wavenumber. The non-zero wavenumbers are found to be amplified in the rear part of the blade at the boundary between the low- and high-speed regions associated with the wakes.* [DOI: 10.1115/1.4056108]

*Keywords: boundary layer development, computational fluid dynamics (CFD)*

## 1 Introduction

The study of the laminar-turbulent transition process occurring in the boundary layers over low-pressure turbine (LPT) blades is of great interest since it has a significant impact on the overall performance of the turbine [1]. In a turbine, the boundary layer is usually exposed to elevated level of freestream turbulence (FST) and periodically passing wakes generated by the upstream blades. The suction side of the blades is subjected to strong pressure gradients. All these factors contribute to the generation of a complex flow inside the boundary layer. Specifically, a wide range of frequencies in the flow can be identified: low frequencies are associated with the wakes shed from the upstream blades, while high stochastic frequencies can be found both in the wake and in the freestream. Different transition scenarios can be observed since, in addition to the inherent instabilities, the boundary layer is forced by the FST and the wake shed by upstream blades. The wake itself is characterized by different parameters such as the flow coefficient and the reduced frequency. In the works by [2–4], the dynamic of the wake migrating in the blade passage has been described. Because of the velocity gradients, the wake once it enters the passage, gets stretched and bowed and is pushed toward the suction side. During this process, we can observe the formation of large vortical structures, which are associated with the generation of strong turbulent fluctuations. This process causes the boundary layer to experience a periodic wake-induced transition [2,5].

On the rear part of the suction side of the LPT blade, the presence of a strong adverse pressure gradient can lead to a separation of the boundary layer. In that case, the transition can be caused by the breakup of Kevin–Helmholtz (KH) modes. The Klebanoff modes generated by the wake can also interact with the separation bubbles and excite short-span KH structures that can cause transition [6,7]. The presence of the separation bubbles and consequently of the KH modes can depend on the FST intensity and the characteristics of the wake. In fact, high level of FST can suppress the flow separation as observed in Refs. [8–12]. At high level of FST, the transition is often caused by the breakdown of the streaks, also called Klebanoff modes, formed either due to high FST intensity

[1]Corresponding author.

Contributed by International Gas Turbine Institute (IGTI) of ASME for publication in the Journal of Turbomachinery. Manuscript received August 9, 2022; final manuscript received September 19, 2022; published online November 25, 2022. Tech. Editor: David G. Bogard.

  

or forced by turbulence carried by upstream wakes. These structures are initially generated at the leading edge of the blade where the shear sheltering process described in Ref. [13] takes place. In this process, the structures with low frequencies penetrate the boundary layer while the high-frequency ones are damped. Once these high- and low-speed streaks are generated, they grow algebraically. Eventually, the breakdown can occur caused by a sinuous and/or varicose secondary instability mechanism. This process has been extensively investigated for simplified geometries [14–18] while the detailed mechanisms have been less studied in the case of an LPT blade. In particular, the transition scenario in the presence of both high level of FST turbulence and incoming wake requires to be further understood. Results reported by Lengani et al. [19] show that the presence of the wake promotes an earlier growth of the streaks compared to the case where only high FST is present. Similar conclusions were drawn by Ref. [20] for a simplified geometry studied through large eddy simulations. The parameters characterizing the unsteady wake shed from the upstream stage play an important role, both in the development of the boundary layer and, in general, in the overall performance of the rotor-stator system [21]. In fact, depending on the interaction between the wakes, they will induce stronger or weaker vortices in the blade-to-blade passage. Lengani et al. [22] also showed that the wakes inducing stronger vortices in the passage also created streaks with higher amplitudes. The spacing of the streaks instead was found to remain almost the same independently of the wake strength.

In the present work, we perform direct numerical simulations of flow over an LPT blade in the presence of high FST and incoming wakes. The wakes are shed from moving cylinders, which are included in the simulations allowing to completely solve frequency and modes together with the structures shed by the cylinder that force the unsteady transition of the blade suction side boundary layer. The focus of the work is on describing the transition scenario in the presence of both high FST and periodically passing wakes.

## 2 Flow Configuration

The setup of the simulations follows the experiments by [19] who studied the laminar-turbulent transition on an LPT blade in the presence of high level of FST and periodically passing wakes. The wakes were generated by a row of cylinders placed upstream of the turbine blades. The same configuration without the moving cylinders has been investigated by Ref. [12]. To highlight the effects of the impinging wakes, similar flow conditions are used here. In the following, the geometrical and flow parameters are given where all spatial dimensions are scaled with the value of the projection of the chord on the horizontal axis $c_x = 0.095$ m and the velocities with the inlet velocity $U_\infty$.

The wakes are generated by a row of cylinders, having a diameter of $D = 0.0316$, which translate in the $y$ direction at a distance of $d_c = 0.347$ upstream of the blade leading edge. The Reynolds number, based on the chord length $c_x$ and the inlet velocity $U_\infty$, is $\mathrm{Re} = 40{,}000$. This corresponds at $\mathrm{Re} = 70{,}000$ of the experiments in Ref. [19] where the exit velocity and chord were used as reference velocity and reference length respectively which is a common value for cruise operation of small-medium sized engines. The Mach number never exceeds 0.1 in order to preserve the loading distribution between the real operation compressible case and the incompressible case, the blade profile has been scaled with a Prandtl–Glauert like transformation.

The inlet velocity has an angle $\alpha_{in} = 40$ deg with respect to $x$-axis. The blade pitch is $g = 0.8653$ and the cylinders move with a velocity of $\mathbf{v}_c = (0,\ v_c,\ 0) = (0, -1.145, 0)$. The distance between the cylinders is equal to the blade pitch. This gives a period of the cylinders passing a blade being $T = 0.756$ corresponding to the frequency $f_w = 1.323$. Moreover, the flow coefficient is $\Phi = u_{in}/v_c = 0.669$ where $u_{in}$ is the horizontal inlet velocity and the reduced frequency is $f_{red} = f_w\, c_x/|\bar{\mathbf{u}}_{ext}| = 0.83$ where $|\bar{\mathbf{u}}_{ext}| = \sqrt{\bar{u}_{ext}^2 + \bar{v}_{ext}^2}$ which are evaluated at downstream the blade trailing edge at $x = 1.1$. It must be mentioned that, to reduce the computational costs, the spacing of cylinders in our simulations is smaller than that in the experiments which was one and half times the blade spacing. However, the Reynolds number and flow coefficient are exactly the same, while the reduced frequency change from 0.69 to 0.83, and such a small difference is not expected to alter significantly the flow physics.

In the present simulations, the computational domain includes only one turbine passage with one moving cylinder.

## 3 Numerical Approach

In this section, we describe the numerical method and the computational setup used in the present work.

**3.1 Equations and Discretization.** We assume the flow evolution is described by the Navier–Stokes equations for an incompressible fluid, since the Mach number in the whole blade passage never exceeds 0.1

$$\frac{\partial \mathbf{u}}{\partial t} + \mathbf{u}\cdot\nabla\mathbf{u} = -\nabla p + \frac{1}{\mathrm{Re}}\nabla^2\mathbf{u} - \chi\mathcal{H}(\mathbf{u}), \quad \nabla\cdot\mathbf{u} = 0, \tag{1}$$

where $\mathbf{u} = (u, v, w)^T$ is the velocity vector, $p$ the pressure, $\mathcal{H}$ a high-pass spectral filter and $\chi$ a model parameter. The filter $\mathcal{H}$ is the same as the one used by Refs. [23,24] which has been proven reliable in describing the flow features involved in the transition process. For the details of the filter, we refer the readers to Ref. [25].

The governing equations (1) are solved in the weak form using a spectral-element method [26] employing the open-source code Nek5000 [27]. The numerical domain is meshed using hexahedral elements. To avoid spurious modes, the $P_N - P_{N-2}$ formulation [28] is employed. Within each element, the velocity field is discretized using Lagrange interpolants on $N_p + 1$ Gauss–Lobatto–Legendre nodes while $N_p - 1$ Gauss–Legendre nodes are used for the pressure. In the present work, we have used the polynomial order $N_p = 9$. To advance the equations in time, the nonlinear terms are treated explicitly using a third-order extrapolation scheme (EXT3), whereas, for the viscous ones, a third-order backward differentiation scheme (BDF3) is employed.

**3.2 Moving Cylinder.** For the purpose of our simulations, we have modified the Nek-Nek tool already implemented in Nek5000 that allows us to run simulations with two overlapping grids. The original implementation is described in Ref. [29], and it has been used to study the effect of impinging wake turbulence on the dynamic stall of a pitching airfoil in Ref. [30]. The advantage of the present method is maintaining spectral accuracy while keeping a strong linear scaling [29] which are two important features of the original code Nek5000. Here, we simultaneously run one simulation in the reference frame of the moving cylinder and another in the reference frame of the stationary blade. The two simulations interact with each other through the Dirichlet boundary conditions at the outlet of the cylinder domain and inlet of the blade domain (dashed and solid red lines in Fig. 1).

The existing method for overlapping grids in Nek5000 has been modified to correctly take into account the two different frames of reference. The value on the interface in the original method is obtained by performing Lagrangian interpolation on the solution of each domain on the grid of the other one. In the present work, we need to take into account that simulations are performed in two different frames of reference. This means that if we, for example, need to know the value of inflow velocity to be imposed at a point $P_b = (x_1,\ y_1,\ z_1)$ on the inlet of the computational domain for the turbine blade, we need to perform the following steps:

(1) compute the coordinate of $P_b$ in the reference frame of the cylinder ($P_c$) at each time-step,
(2) perform interpolation to obtain the velocity at $P_c$ in $\Omega_c$. This step relies on the method described in Ref. [29] and is already implemented in Nek5000,

(3) correct the interpolated velocity by adding the translation velocity $\mathbf{v}_c$ of the domain $\Omega_c$ to be used as the inlet velocity in the simulation of the turbine blade.

At step (1), the only coordinate to be updated is the $y$-coordinate since the velocity of the cylinder is zero in the other directions. This can be done using the following relation:

$$y_{1c} = \mathrm{mod}(y_1 - v_c\, t,\, g) + y_{\min} \tag{2}$$

where $g$ is the blade pitch and $y_{\min}$ is the $y$-coordinate of the lowest point on the interface. The mod operation returns the remainder of the division between the term $y_1 - v_c\, t$ and the term $g$. A similar procedure is applied to compute the values of the velocities on the outflow boundary of the domain $\Omega_c$ for the simulation of the flow over the moving cylinder. Here, a third-order time integration with IEXT3 at interface boundaries is used. For the sake of numerical stability, three inter-grid iterations per time-step are used [31]. This means that each time-step is repeated three times, and at each time, the values on the interface boundaries are updated.

**3.3 Computational Domains and Grids.** Figure 2 shows the distribution of the spectral elements in the $xy$-plane for both meshes. The spanwise width of the domain is $L_z = g/2$. In the mesh for the turbine blade, the inlet is located at $x = -1.05$, while the outflow is found at $x = 1.6$ (the blade leading edge corresponds to $x = 0.0$). The mesh for the cylinder counts 113, 610 spectral elements, while the one for the turbine has 134, 340 elements. For the turbine blade, the element distribution at the wall is close to the one used in Ref. [12] where the grid convergence was checked. In particular, we have around the turbine blade the tangential spacing $\Delta\xi^+ < 17.0$, the wall-normal $\Delta\eta^+ < 0.4$ and the spanwise $\Delta z^+ < 7.0$. The same spanwise spacing is used for the cylinder's domain while on its surface we have a tangential spacing $\Delta\xi^+ < 6.0$ and a wall-normal $\Delta\eta^+ < 0.6$.

**3.4 Boundary Conditions.** In Fig. 1, a schematic representation of the numerical setup is shown. Here, the dashed lines refer to the numerical domain of the cylinder while the solid ones to that

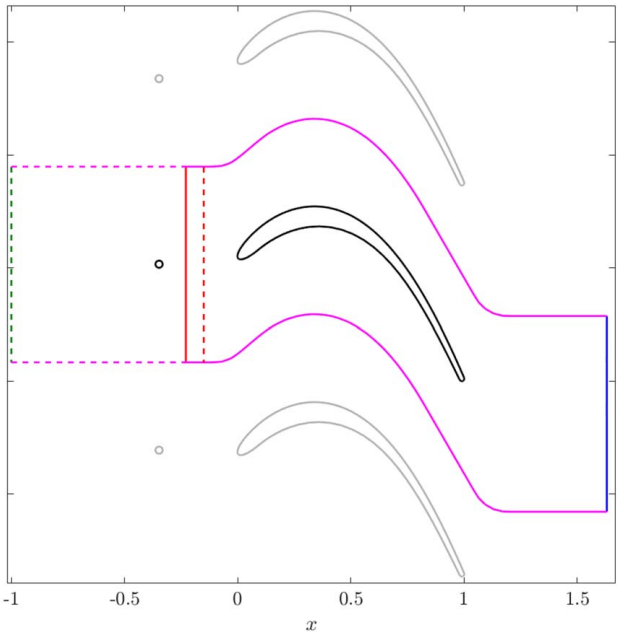


**Fig. 1 Sketch of the numerical domains. Dashed lines belong to the computational domain for the cylinder ($\Omega_c$), solid lines to that for the turbine blade ($\Omega_b$). No-slip boundary conditions are imposed along the black lines, periodic conditions along the magenta lines, inlet Dirichlet condition along the green line, outflow condition along the blue line, and coupling Dirichlet condition along the red lines.**

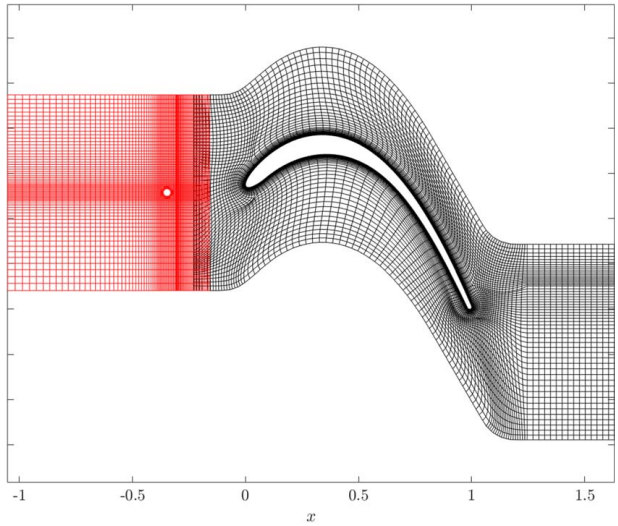


**Fig. 2 Spectral element distribution in the $xy$-plane**

of the blade. As mentioned earlier, we run two separate simulations, one for the cylinder and the other for the turbine blade, coupled through their inflow/outflow conditions along the red lines (see Sec. 3.2). At the inlet (dashed green line), Dirichlet boundary condition is used. The inlet velocity profile is $\mathbf{u}_{in} = (\cos(\alpha), \sin(\alpha), 0)$ to which we superimpose randomized Fourier modes to generate the FST (see Sec. 3.5). Black lines in the figure represent the surface of the cylinder and of the turbine blade where a no-slip condition is imposed. On the upper and lower boundaries (magenta lines) and the boundaries in the spanwise direction, a periodic boundary condition is used. On the outflow of the turbine domain, stress-free boundary conditions are applied.

**3.5 Generation of Freestream Turbulence.** As previously stated, the incoming flow is subjected to freestream turbulence. This is done by prescribing a superposition of Fourier modes with a random phase shift at the inlet of the domain. With the aim of having homogeneous and isotropic turbulence, we divide the wavenumber space into 80 concentric shells, where each shell represents the amplitude associated with a given wavenumber. Forty points are randomly chosen on each shell to obtain the components of the wavenumber vectors. At this point, we scale the modes so that their amplitudes match the von Kármán spectrum. The method is described in detail in Ref. [32] with the main difference that here, instead of the modes from the continuous spectrum of the Blasius flow, the Fourier modes are used. The same method has been used by Ref. [12] to generate FST of different intensities. The FST intensity is chosen to be $Tu = 5.2\%$ at the blade leading edge which corresponds to the high FST case in [12]. In the present simulation, an integral length scale of $\Lambda = 0.105$ is used. This value is slightly lower than that of Ref. [12]. However, it is not expected to alter the flow

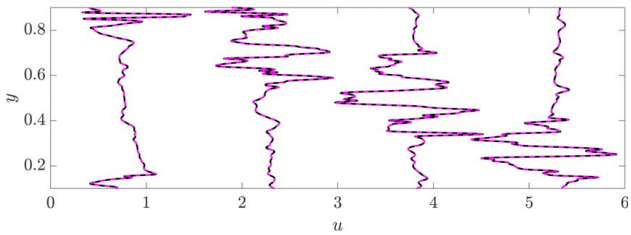


**Fig. 3 Axial velocity profiles at $z = 0.0$ and $x = -0.2$ and $t = \{t_0, t_0 + 0.25T, t_0 + 0.5T, t_0 + 0.75T\}$. The profiles are shifted according to $u_k = u + 1.5\,(k-1)$. Black lines represent the velocity extracted from the turbine domain, and magenta lines represent the velocity extracted from the cylinder domain.**

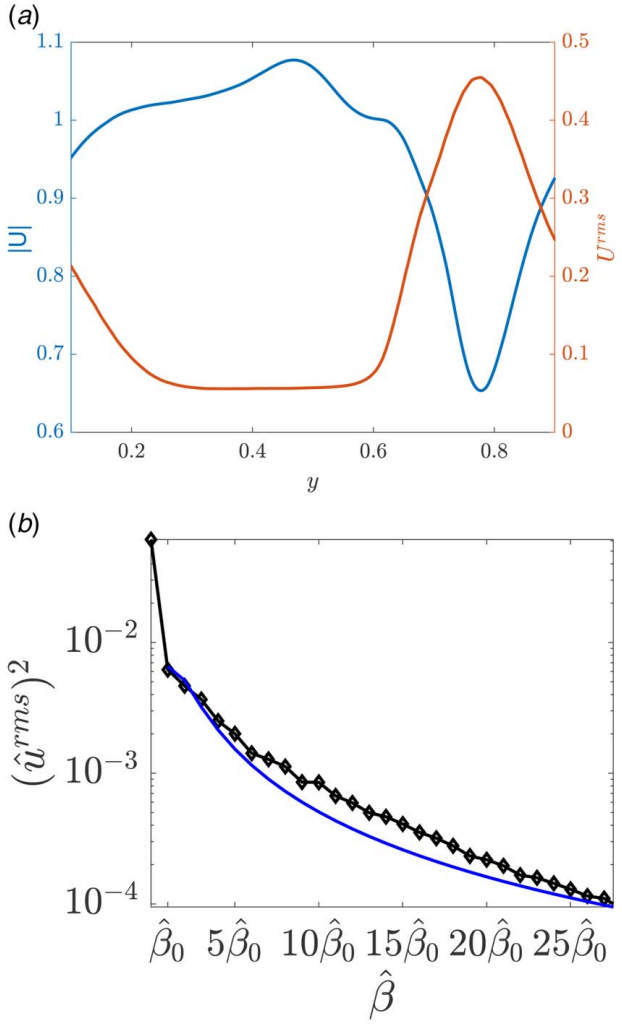


**Fig. 4 (*a*) Absolute value $|\bar{U}|$ and $U^{rms}$ at $x = -0.2$ and (*b*) spanwise spectrum at $x = -0.2$ and positions of max($\hat{u}^{rms}$) ($y = 0.779$, black) and the scaled von Kármán spectrum (blue)**

physics since the transition process of the unsteady case is dominated by the turbulence carried by wakes, as discussed in Berrino et al. [33].

## 4 Results

In the following, we first present the validation of our implementation of moving bars. Then, the behavior of the time-averaged flow is discussed, and results are compared with those from Ref. [12] who investigated a similar flow case in the absence of the moving

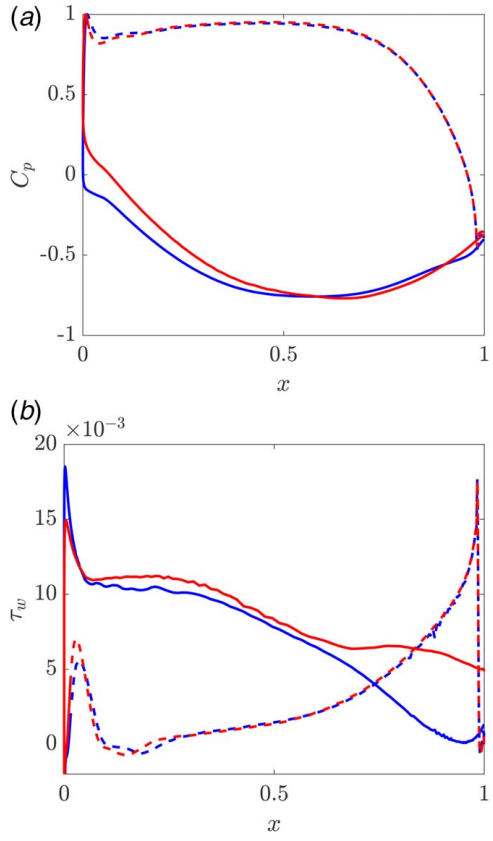


**Fig. 5 (*a*) Pressure coefficient and (*b*) wall shear stress distribution for the homogeneous-turbulence (blue) and moving bars case (red). Solid lines are used for the suction side, and dashed lines for the pressure side.**

bars. Finally, the time evolution of the flow is discussed and features of the boundary-layer perturbations are analyzed in detail.

**4.1 Validation of Moving Mesh Implementation.** To check the implementation, the values of the instantaneous velocity $u$ at $z = 0$ and $x = -0.2$ at different time-steps are extracted from the two computational domains. Then the algorithm previously described is applied so that a comparison is possible. The results for four time-steps separated by 0.25 $T$ are shown in Fig. 3. We can see that the two profiles match showing the correct implementation of the method we employed.

**4.2 Meanflow.** In this section, the flow quantities averaged over 12 cylinder passages are presented and compared with the

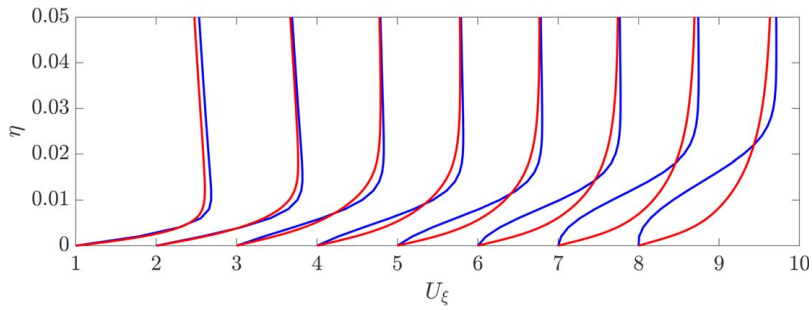


**Fig. 6 Mean tangential velocity profiles on the suction side of the blade for homogeneous-turbulence (blue) and moving bars case (red). The profiles are shifted according to $\bar{u}_{\xi_k} = \bar{u}_\xi + k$ with $k = 1, 2, \ldots, 8$. The profiles are extracted at $x \in \{0.2, 0.5, 0.7, 0.75, 0.8, 0.85, 0.9, 0.95\}$.**

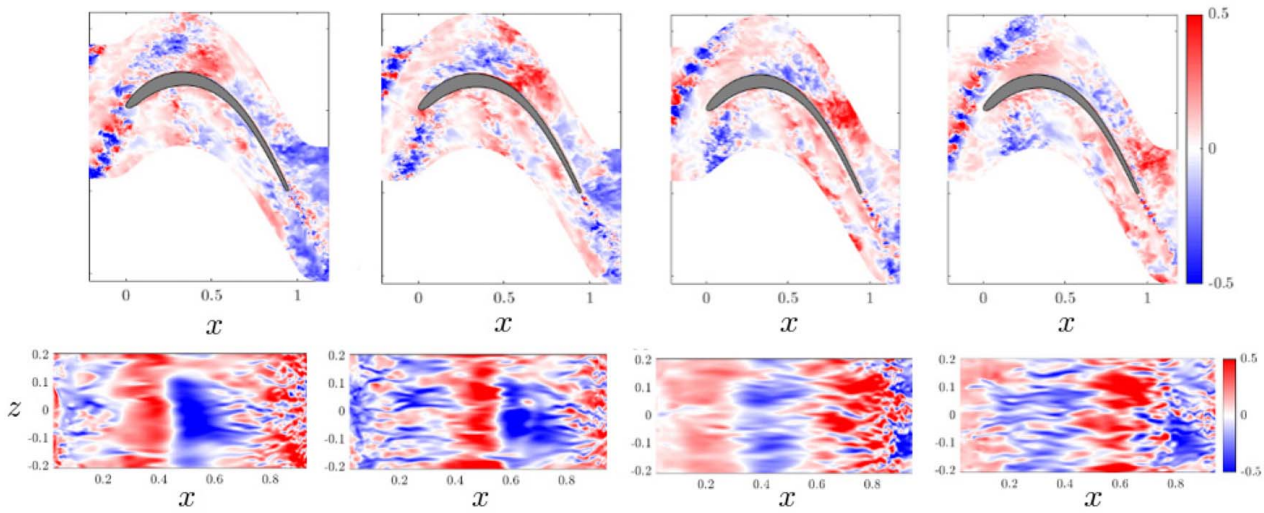

**Fig. 7 First row: blade-to-blade view of the axial velocity perturbation field, $\hat{u}$. Second row: tangential velocity perturbation field, $\hat{u}_\xi$, at wall normal distance $\eta = 0.005$. From left to right, the time increases as $t \in \{t_0, t_0 + 0.25\ T, t_0 + 0.5\ T, t_0 + 0.75\ T\}$.**

results of Ref. [12] who studied a similar case without moving cylinders (referred to as the homogeneous-turbulence). The results highlight the effects of the wake shed from the cylinders on the development of the statistical properties of the boundary layer.

First, the flow behind the moving cylinder is shortly described since it acts as an inflow condition to the LPT blade. The presence of the cylinder generates a wake which is associated with lower momentum and strong fluctuations (Fig. 4(*a*)). These reach values of $U^{\text{rms}} \approx 0.45$ which are significantly higher than what we observe outside the wake region. In order to further characterize the flow in the wake, Fourier series of the streamwise velocity in the spanwise direction has been computed. The analysis has been performed at outlet section of the cylinder domain at $y$ coordinates corresponding to the position of maximum $\hat{u}^{\text{rms}}$. The results of the analysis are presented in Fig. 4(*a*) together with the scaled von Kármán spectrum used to generate the FST at the inlet of the domain. As shown, the spectrum inside the wake has a similar shape to the von Kármán one. Therefore, it appears that the presence of the cylinder does not significantly affect the fluctuating energy distribution among the different spanwise wavenumbers having $\hat{\beta} > 0$. Note instead that the high root-mean-square (rms) value for the wavenumber zero is introduced by the cylinder and it is the trace of the von Kármán vortex. Finally, because of the loss of momentum caused by presence of the moving cylinder, the mean velocity upstream of the blade is reduced of 4.4% with respect to the one prescribed at the inlet.

In Fig. 5(*a*), the distribution of the pressure coefficient ($C_p$) for the clean-inlet and moving-bar cases is presented. The pressure

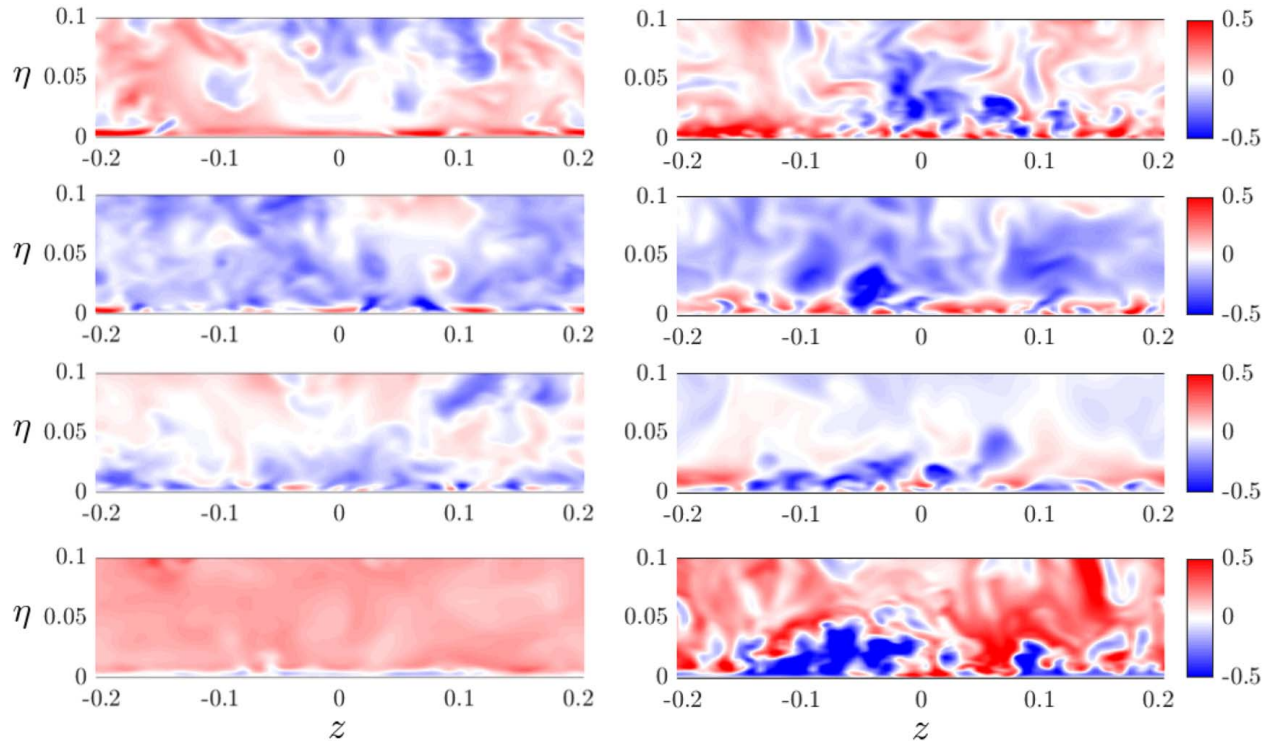

**Fig. 8 Tangential velocity perturbation field, $\hat{u}_\xi$, in the wall-normal plane at $x = 0.3$ (left column) and $x = 0.9$ (right column). From top to bottom, time increases $t \in \{t_0, t_0 + 0.25\ T, t_0 + 0.5\ T, t_0 + 0.75\ T\}$.**

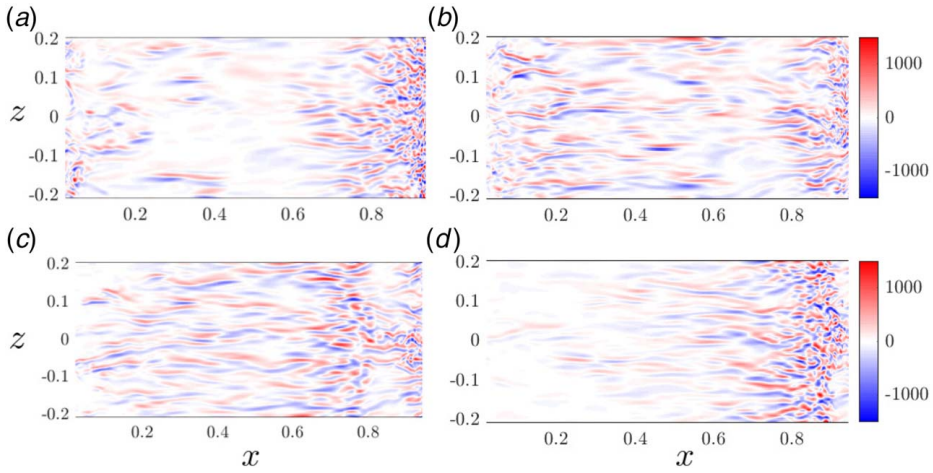


**Fig. 9 Wall-normal vorticity field at $\eta = 0.005$ and different time instances $t \in \{t_0, t_0 + 0.25\ T, t_0 + 0.5\ T, t_0 + 0.75\ T\}$ shown in (*a*), (*b*), (*c*), and (*d*), respectively**

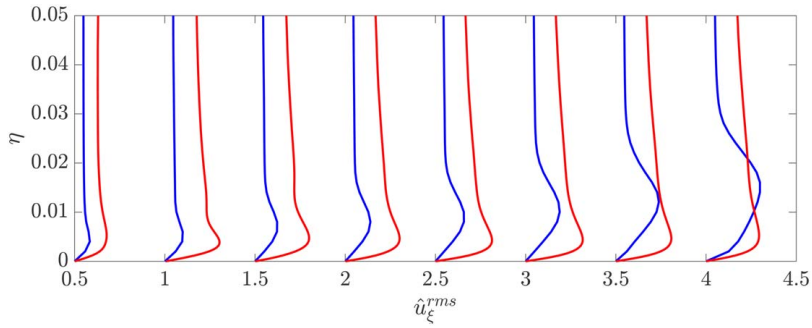


**Fig. 10 RMS of the tangential velocity perturbations on the suction side of the blade for homogeneous-turbulence (blue) and moving bars case (red). The profiles are shifted according to $\hat{u}_{\xi_k}^{rms} = \hat{u}_\xi^{rms} + 0.5\,k$ with $k = 1, 2, \ldots, 8$. The profiles are extracted at $x \in \{0.2, 0.5, 0.7, 0.75, 0.8, 0.85, 0.9, 0.95\}$.**

coefficient is computed as $\mathbf{C_p} = (\mathbf{P} - \mathbf{P_{in}})/\mathbf{P_{dyn_{in}}}$ where the $P_{in}$ and $\mathbf{P_{dyn_{in}}}$ represent the static and the dynamic pressures computed at $x = -0.15$, respectively. As shown, on the pressure side of the blade, the passing wakes do not significantly alter the pressure distribution. This is not the case on the suction side of the blade. For $x < 0.5$, the pressure in the homogeneous-turbulence reaches lower values. This behavior is a consequence of the variation of the angle of attack between $\alpha_{in} = 40$ deg and $\alpha_{in} = 36.4$ deg due to the presence of the wakes. The two pressure distributions both reach a minimum for $x \approx 0.6$ and then follow the same behavior until the end of the blade where the homogeneous-turbulence again assumes higher values. In Fig. 5(*b*), the distribution of the wall shear stress, $\tau_w$, around the blade is shown. Also, in this case, the differences between the two cases are small on the pressure side. It can be observed that the length of the recirculation bubble developing just downstream of the blade leading edge is slightly smaller in the unsteady case. Once the flow is reattached, the two cases have very similar values of shear stress. On the suction side, shortly after the leading edge, the shear stress in the moving bars case assumes higher values than in the clean-inlet one. This is due to the periodic forcing of the turbulence carried by wakes that locally increases the shear stress also in the accelerating part of the suction side. Up to $x \approx 0.6$, $\tau_w$ shows the same behavior in the two cases. In the region of adverse pressure gradient instead, the shear stress decreases in the homogeneous-turbulence, while in the moving bars case, it remains almost constant. Particularly, in the homogeneous-turbulence, the boundary layer is prone to separation close to the blade trailing edge, while the presence of upstream wake forces a prompter transition process of the boundary layer that avoids separation.

In Fig. 6, the tangential velocity profiles, $\bar{u}_\xi$, extracted at different streamwise positions on the suction side of the blade are presented. As shown, the profiles at locations close to the leading edge are similar to those in the homogeneous-turbulence but reaching slightly higher values in the freestream as expected from the $C_p$ distribution. Further downstream, the clean inlet-case profiles get closer to a separated flow profile. However, the flow does not reach such conditions since the wall shear stress remains weakly positive. The situation is quite different in the simulations with the moving bars where the boundary layer profiles are fuller. This difference is also visible in Fig. 5(*b*) where the wall shear stress in the moving bars case shows higher values close to the trailing edge.

**4.3 Instantaneous Flow Features.** In this section, we discuss the effects of the migration of the wake shed by the moving bars on the boundary layer. We first discuss the instantaneous flow field extracted at different phases of the cylinder period. Here, we have selected fields separated by $\Delta t = 0.25\ T$ where $T = g/v_c$ is the period of the moving bars. In particular, we will focus on the evolution of the perturbation field $\hat{\mathbf{u}} = \mathbf{u} - \bar{\mathbf{u}}$, where bar denotes the time-span-averaged values.

In Fig. 7, snapshots of the axial perturbation velocity $\hat{u}$ in a *xy*-plane are shown in the upper row. The first frame corresponds to a time instance where the wake hits the leading edge of the blade. This generates a region of negative perturbation velocity on the suction side of the blade, in front of which there is a region of positive perturbation velocity, as shown in the subsequent frame. These two regions are then advected toward the trailing edge while the next wake approaches the blade and eventually hits it

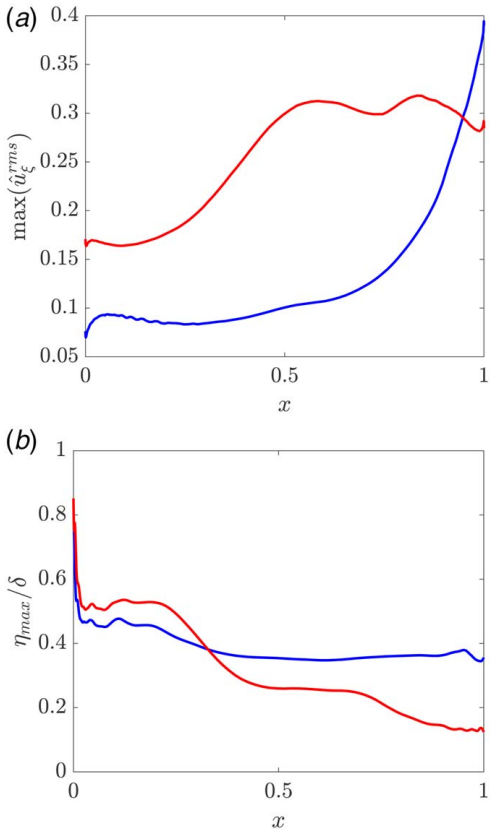


**Fig. 11 (*a*) Maximum RMS of tangential velocity in wall normal direction and (*b*) its wall-normal location as a function of the chord position. The wall-normal location scaled with the boundary-layer thickness is given in (*c*). Blue lines represent the homogeneous-turbulence and red lines represent the moving bars case.**

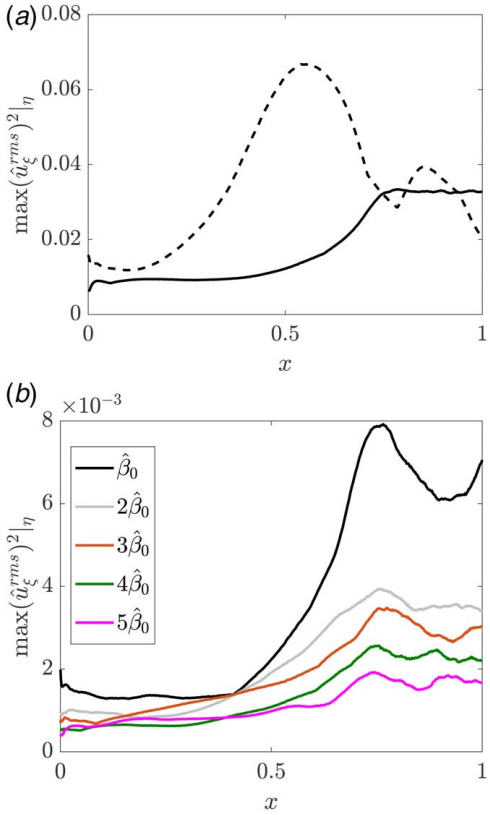


**Fig. 12 (*a*) Contribution to $\max(\hat{u}_\xi^{rms})^2|_\eta$ for the spanwise wavenumber $\hat{\beta} = 0$ (black dashed line) and for $\hat{\beta} > 0$ (black solid line) and (*b*) $\max(\hat{u}_\xi^{rms})^2|_\eta$ for different spanwise wavenumbers**

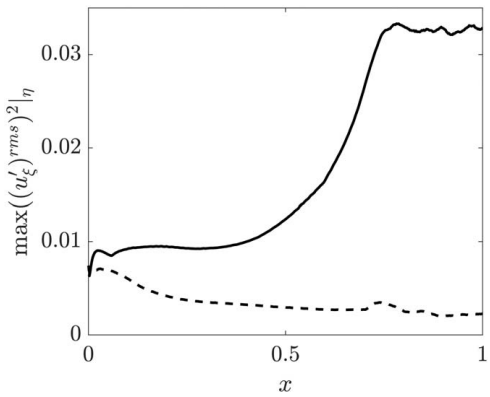


**Fig. 13 Contribution of spanwise wavenumber $\hat{\beta} = 0$ (dashed line) and for $\hat{\beta} > 0$ (solid line) to $\max((u'_\xi)^{rms})^2|_\eta$**

again. In particular, it can be noticed that the positive perturbation region reaches the highest value after the middle of the blade, which corresponds well to the location of maximum $\hat{u}_\xi^{rms}$, as will be discussed later.

This periodic impingement of the wakes affects the generation and development of perturbations inside the boundary layer, as also shown by the statistical quantities discussed in Sec. 4.4. To further highlight this, the tangential perturbation velocity fields, $\hat{u}_\xi$, on the suction side at a wall distance $\eta = 0.005$ are shown in the bottom of Fig. 7. Also, here, we can recognize the footprint of the alternating positive and negative velocity perturbation regions inside the boundary layer. In the bottom panel of Fig. 7, approximately in the area $0.2 < x < 0.6$, a region of high-velocity perturbation followed by one with low-velocity perturbation are clearly recognizable. The development of these two regions can be followed as they travel towards the trailing edge. In the first instant, the wake has just hit the turbine blade. From that point, a region of low-speed perturbation is created inside the boundary layer. This region is strongly modulated in the spanwise direction due to the high level of turbulence inside the wake. The streaky structures are generated and advected downstream as the low-velocity perturbation region moves towards the trailing edge. These streaks have a relatively long streamwise wavelength in most of the domain, but they break down into smaller scales around $x \approx 0.7$. When the cylinder wake has moved away from the blade, the strength of the streaks close to the leading edge decays, and the flow becomes almost spanwise homogeneous in that area, but as soon as the following wake reaches the blade, the process of streak generation gets repeated. Thus, the present direct numerical simulation (DNS) data make evident that streaky structures start to be periodically generated from the leading edge region. The streaky structures are also clearly visible in Fig. 8 where the tangential perturbation velocity fields in the $yz$-plane at $x = 0.3$ and $x = 0.9$ are plotted. In addition to the boundary-layer perturbations, the freestream perturbations migrating in the blade passage are visible there. In particular, the second and fourth rows of Fig. 8 clearly show the passage of the low- and high-speed perturbations, respectively which are induced by the large scale structures carried by wakes. In all of the snapshots at $x = 0.9$, close to the wall ($\eta < 0.01$), alternating low- and high-speed structures are visible. At $x = 0.3$ instead streaks are visible in (*c*) and (*e*) while in (*a*) and (*g*) only a mild spanwise modulation is visible. This suggests that closer to the trailing edge, the disturbances having a non-zero spanwise wavenumber are stronger, as it will be shown in the following. Being the advection velocities different along the wall-normal direction, in Fig. 8, the last frame for $x = 0.9$ shows that the velocity

fluctuations close to the surface have negative values while the free-stream is mostly characterized by positive perturbations. The opposite scenario is instead observable for $t = t_0 + 0.25\Delta T$.

To better visualize the boundary-layer structures, the wall-normal vorticity extracted at a distance $\eta = 0.005$ from the surface is shown in Fig. 9 for different time instances. At all time instances, streamwise elongated structures can be recognized. These type of structures were also observed in Ref. [12] for the homogeneous-turbulence. The effects of the perturbations generated by the wake of the cylinder are also visible. As mentioned earlier, once the region of positive streamwise fluctuations velocity reaches the rear part of the blade (see also Fig. 7), finer vortical structures are formed, which are due to the breakdown process.

**4.4 Characteristics of the Boundary Layer Perturbations.** As a first step to investigate the behavior of disturbances in the boundary layer, we compute the RMS values of the tangential velocity perturbations, $\hat{u}_\xi^{\text{rms}}$, and compare them with those obtained for the homogeneous-turbulence (the high FST case in Ref. [12]). The $\hat{u}_\xi^{\text{rms}}$ profiles in the wall-normal direction extracted at different streamwise positions are shown in Fig. 10. As can be seen there, the presence of the wake increases the disturbance level significantly far away from the blade surface. In the moving bars case, the shape of the velocity profiles stays similar along the blade, while for the homogeneous-turbulence the peak of fluctuation moves far away from the wall approaching toward the blade trailing edge.

In Fig. 11(*a*), the variation of max ($\hat{u}_\xi^{\text{rms}}$) in wall normal direction as a functions of $x$ is given for the suction side of the blade. A general observation is the higher level of perturbations, almost over the whole blade, in the presence of the moving bars. Further, it can be observed that in the homogeneous-turbulence, the maximum RMS value of the perturbations increases rapidly in the region of the adverse pressure gradient, $x > 0.5$. While in the moving bars case, the rapid disturbance growth starts already around $x = 0.2$ and then saturates around a value of 0.3 in the region $x > 0.5$.

In Fig. 11(*b*), the wall-normal position of the maximum $\hat{u}_\xi^{\text{rms}}$, denoted as $\eta_{\max}$, scaled with the local boundary-layer thickness are presented for the suction side. We can see that in the homogeneous-turbulence, for $x > 0.4$, we have almost a constant value, meaning that the growth of $\eta_{\max}$ follows the one of the boundary layers. For the moving bar case, this behavior is found only between $0.45 < x < 0.65$ while at other streamwise locations along the chord, the value of $\eta_{\max}/\delta$ decreases.

To better characterize the boundary-layer perturbations involved in the transition process, a Fourier decomposition of the disturbance field **u** is performed. Here, we first compute the fast Fourier transform of the flow field in the spanwise direction at 1200 time instances. In this way, we obtain the spanwise Fourier coefficients, function of $x$, $y$, for all the time realizations. These are then used to calculate the RMS values of each Fourier mode. Results of the analysis are presented in Fig. 12, where the contributions of different spanwise wavenumbers, $\hat{\beta}$, are given.

The contribution of the spanwise homogeneous perturbations, $\hat{\beta} = 0$, and other wavenumbers are reported separately in Fig. 12(*a*). In the homogeneous-turbulence contribution to the fluctuating velocity with $\hat{\beta} = 0$ was negligible (not shown here). This is radically different in the moving bars case, as can be seen in this figure. The presence of the wake results in the strong fluctuations associated with $\hat{\beta} = 0$ (i.e., wake effects are uniform in the spanwise direction), which gives the major contribution to the velocity fluctuations up to $x \approx 0.7$. The total contribution of the wavenumbers $\hat{\beta} > 0$ is, in fact, smaller over the entire blade up to this location.

The RMS amplitude of different Fourier modes is shown in Fig. 12(*b*). The extension of the computational domain in the spanwise direction is $L_z = g/2 = 0.4326$, which gives the smallest wavenumber in the computations being $\hat{\beta}_0 = 2\pi/L_z = 14.52$. This mode has the largest amplitude all along the suction surface and is the totally dominating one for $x > 0.7$. The contributions of the other modes appear to decrease with the increasing wavenumber, as also observed for the homogeneous-turbulence (not shown here). The amplitudes of all higher modes increase up to $x > 0.7$ and then start to be approximately constant. The amplitude distribution among the different wave numbers shows the same behavior as the inlet spanwise spectrum reported in Fig. 4(*b*). The small spanwise wavenumber has the largest energy, that decrease for larger wavenumbers, this means that the spectrum in the freestream strongly affects the distribution of the energy in the boundary layer.

**4.5 Phase-Averaged Flow.** In order to further investigate the effects of the periodic cylinder wakes on the boundary layer, we split the perturbation field $\hat{\mathbf{u}}$ in the time-harmonic ($\tilde{\mathbf{u}}$) and random parts ($\mathbf{u}'$) following [34], where the time-harmonic field $\tilde{\mathbf{u}}$ is the contribution associated with the periodic passage of the wakes and $\mathbf{u}'$ the stochastic perturbations caused by the freestream turbulence and by structures carried by wakes.

To separate contribution of these two quantities, we phase averaged according to

$$\langle f(\mathbf{x}, t)\rangle = \frac{1}{ML_z}\sum_{m=0}^{M}\int_{-L_z/2}^{L_z/2} f(\mathbf{x}, t + mT)\,\mathrm{d}z, \tag{3}$$

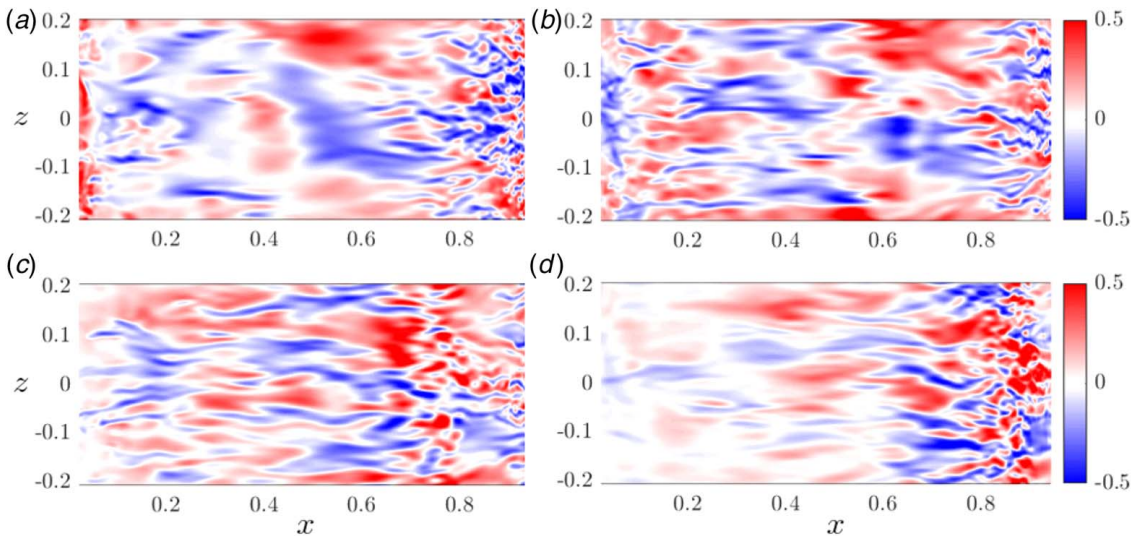


**Fig. 14 Stochastic tangential perturbation field, $u'_\xi$, at $\eta = 0.005$ for different time instances $t \in \{t_0, t_0 + 0.25\,T, t_0 + 0.5\,T, t_0 + 0.75\,T\}$ shown in (*a*), (*b*), (c), and (*d*), respectively**

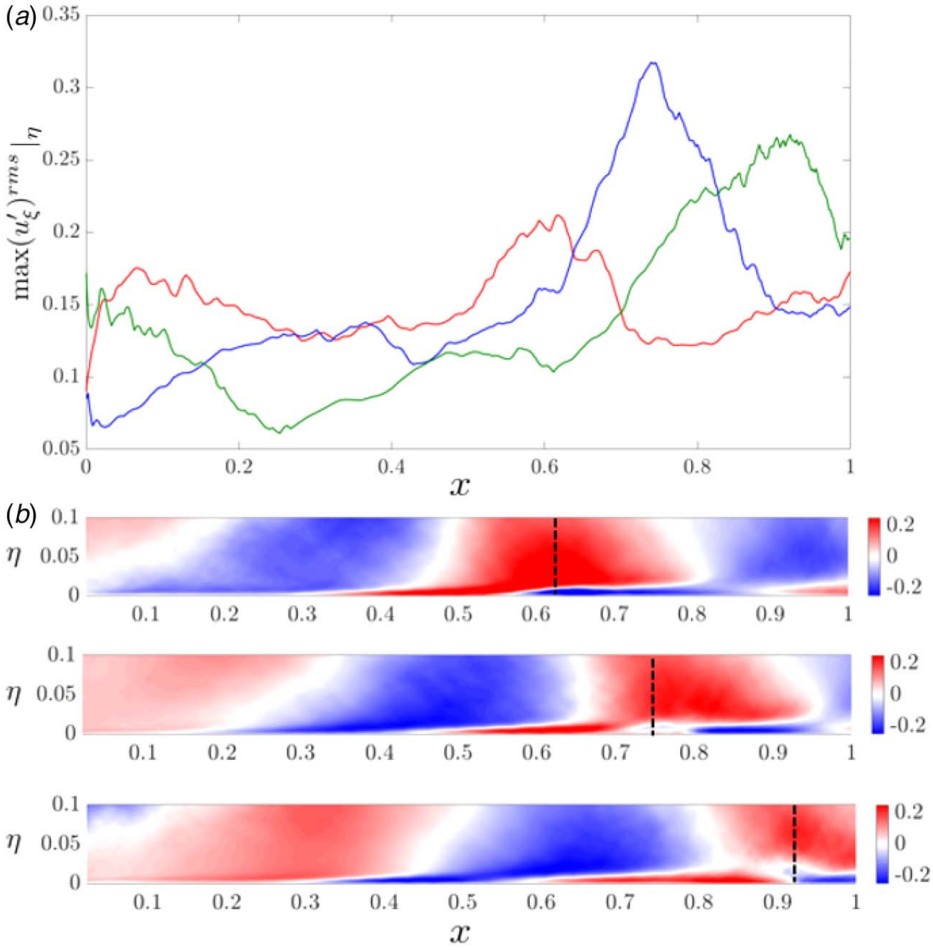


**Fig. 15 (*a*) The maximum RMS values of $u'_\xi$ in wall normal direction computed using the velocity fields with the same phase for 0.25*T* (red line), 0.5*T* (blue line), and 0.75*T* (green line) and (*b*) the phase-averaged $\tilde{u}_\xi$ fields extracted at the same phases as in (*a*). Dashed black lines correspond to the position of the maximum value of the RMS.**

In the present work, the number of periods used in the phase averaging is $M = 15$. The above definition yields $\mathbf{u}' = \mathbf{u} - \langle \mathbf{u} \rangle$.

We first compute the RMS values associated with different spanwise wavenumbers of the stochastic perturbations $u'$ proceeding as previously done for $\hat{u}$. Notice that since $\tilde{u}$ is invariant in the spanwise direction, the RMS of the non-zero wavenumbers of $u'$ is the same as the one of $\hat{u}$. This is clearly shown by comparing results presented in Fig. 13 with those in Fig. 12(*a*). The contribution of $\hat{\beta} = 0$ appears to be much smaller than for $\hat{u}$, showing that the oscillations of the zero wavenumber are, for the most part, due to the passing wakes.

The $u'_\xi$ field extracted at the wall distance $\eta = 0.005$ is shown in Fig. 14 for different time instances in the wake passing period. Here, one can clearly see the presence of the streaks but no traces of the large regions with positive and negative perturbation velocities observed for $\hat{u}_\xi$ (see Fig. 7). This is consistent with the Fourier analysis of the stochastic perturbation field.

A noticeable behavior of the stochastic velocity field is the decay of perturbation amplitude in the region $x < 0.6$ at $t = 0.75T$, see Fig. 14(*d*). At this time instance, the cylinder wake has already passed the leading edge of the blade, and the next one has not reached it yet. The streaks in the front part of the blade are still present but they are weaker than at other time instances since the magnifying effect of the wake is at its minimum. The strong structures seen at $x > 0.6$ are those generated at earlier time instances and advected downstream. The rear front of them corresponds to the location where the boundary between two consecutive large negative and positive perturbations are found in Fig. 7. In order to confirm this observation, we compute the RMS values of $u'_\xi$ using the fields having the same phase and not all the fields as previously done. The results of the analysis are presented in Fig. 15 together with the harmonic part of the tangential velocity perturbations, $\tilde{u}_\xi$, to better understand the influence of the migrating wakes on the random fluctuations. What observed in Fig. 14 is confirmed. In fact, Fig. 15 clearly shows that the maximum RMS values are found in the second part of the blade at the boundary between the low- and high-speed region. Therefore, we clearly observe how the periodic migration of the wakes influences the generation of streaks. In particular, in the second part of the blade, the wakes shed from the moving cylinder is tilted and pushed towards the suction side (Fig. 7) interacting with the boundary layer. As a consequence, a strong growth of the stochastic perturbations takes place on the suction side which can be observed in Fig. 15(*a*).

## 5 Summary and Conclusions

In the present work, the evolution of the disturbances in the boundary layer over a low-pressure turbine blade subject to periodic impinging wakes shed from moving bars upstream of the blade and high level of FST is studied. Understanding the effect that these disturbances have on the transition on the blade is of great importance since it directly affects the performance. The investigation is based on direct numerical simulations in which flow around the blade and the moving cylinders are considered in their respective frame of reference and interact through appropriate boundary conditions. Both the incoming flow and the wake of the cylinders are characterized by a high turbulence level. Except for the presence of the moving bars and a shorter integral length scale of FST, the geometry and

flow conditions correspond to that studied by [12] which is used as the reference to highlight the effects of the periodic passage of the cylinder wakes. The flow characteristics have been analyzed using mean values as well as time- and phase-averaged ones.

The presence of the wake is associated with a region of low-momentum flow exhibiting high-velocity fluctuations. Inspecting the pressure distribution and the wall shear stress, it was observed that the presence of the wakes mainly affects the suction side of the blade. In particular, the pressure on the suction side is slightly increased, which is due to a smaller angle of attack caused by the wakes. For what concerns the shear stress, it is found that, in general, its value is higher compared to the homogeneous-turbulence, especially in the rear part of the blade. In the region of adverse pressure gradient in the homogeneous-turbulence, the boundary layer gets close to separation, and therefore, the shear stress at the wall decreases. In the moving bars case, instead, the boundary layer maintains higher values of velocity close to the wall causing a fuller profile that resists flow separation.

Passage of the wakes generated regions of low- and high-speed perturbations, which were advected through the blade passage. The traces of these regions were clearly visible inside the boundary layer. In general, the perturbation field was found to be dominated by streaky structures. The strength of these streaks varies during a period of cylinder passage. Strong perturbations are created inside the boundary layer when the wake hits the blade leading edge. These perturbations generate the streaks, which then advect downstream. The strength of these streaks, in large part of the boundary layer, decays when the wake has moved away until the next one hits the leading edge and the process gets started again. The presence of elongated structures was also confirmed by the wall-normal vorticity. Its analysis also showed the generation of finer vortical structures in the rear part of the blade once the positive perturbation induced by the wake reached this region.

The detailed analysis of the boundary-layer perturbations showed that the moving bars case exhibits higher RMS values, except at the locations close to the trailing edge on the suction side. The maximum RMS values of $\hat{u}_\xi$ for different spanwise wavenumbers were found to increase with increasing distance from the leading edge up to $x \approx 0.7$ after which they almost saturated. It was observed that the major contribution to the perturbation field is given by those with zero spanwise wavenumber since it is largely associated with the periodic wakes migration. The contribution to the perturbation field of the other wavenumbers decreases as the wavelength of the perturbation reduces. This is consistent with the amplitude of the different wave numbers observed for the spectrum computed upstream of the blade (Fig. 4(*b*)) and this is consistent with what was observed in the case of homogeneous-turbulence. However, even if the migration of the wake does not show a strong impact on amplitude distribution among the different wavenumbers for the stochastic part, it clearly affects its evolution over the blade. In fact, we observed that the stochastic perturbations are periodically excited on the second half of the blade suction side by the migration of the wakes.

## Acknowledgment

The European Research Council provided financial support for this work under grant agreement 694452-TRANSEP-ERC-2015-AdG. The computations were performed on resources provided by the Swedish National Infrastructure for Computing (SNIC) at the PDC Center for High-Performance Computing at the Royal Institute of Technology (KTH) and the National Supercomputer Centre at Linköping University.

## Conflict of Interest

There are no conflicts of interest.

## Data Availability Statement

The datasets generated and supporting the findings of this article are obtainable from the corresponding author upon reasonable request.

## Nomenclature

$g$ = blade pitch
$p$ = static pressure
$t$ = time
$\mathbf{u}$ = velocity vector
$D$ = cylinder diameter
$\mathcal{H}$ = high-pass spectral filter
$T$ = cylinder passing period
$\hat{\mathbf{u}}$ = perturbation velocity vector
$\tilde{\mathbf{u}}$ = harmonic perturbation velocity vector
$c_x$ = axial chord length
$c_f$ = skin friction coefficient $= \tau_w/(0.5\rho U_\infty^2)$
$c_p$ = pressure coefficient $= (p - p_\infty)/(0.5\rho U_\infty^2)$
$d_c$ = axial distance of the cylinders from the blade leading edge
$f_w$ = cylinder passing frequency $= 1/T$
$f_{red}$ = reduced frequency
$v_c$ = cylinder velocity
$\mathbf{u}'$ = stochastic perturbation velocity vector
$L_z$ = domain spanwise length
$U_{in}$ = inflow velocity
Re = Reynolds number
$Tu$ = turbulence intensity
$u, v, w$ = velocity in $x, y, z$ directions
$\alpha_{in}$ = inflow flow angle
$\beta$ = spanwise wavenumber
$\delta^*$ = displacement thickness
$\xi, \eta, z$ = tangential, wall-normal, spanwise coordinate
$\Lambda$ = integral length scale
$\nu$ = kinematic viscosity
$\tau_w$ = wall shear stress
$\rho$ = fluid density
$\Phi$ = flow coefficient
$\chi$ = model parameter

### Superscripts and Subscripts

$+$ = viscous units
$\infty$ = undisturbed, freestream
$ext$ = cascade outlet
rms = root-mean-square
$-$ = mass-averaged quantities
$|_\eta$ = operation performed in wall normal direction

## References

[1] Hodson, H. P., and Howell, R. J., 2005, "The Role of Transition in High-Lift Low-Pressure Turbines for Aeroengines," Prog. Aerosp. Sci., **41**(6), pp. 419–454.
[2] Wu, X., and Durbin, P. A., 2001, "Evidence of Longitudinal Vortices Evolved From Distorted Wakes in a Turbine Passage," J. Fluid. Mech., **446**, pp. 199–228.
[3] Michelassi, V., Wissink, J. G., Frohlich, J., and Rodi, W., 2003, "Large-Eddy Simulation of Flow Around Low-Pressure Turbine Blade With Incoming Wakes," AIAA. J., **41**(11), pp. 2143–2156.
[4] Stieger, R. D., and Hodson, H. P., 2005, "The Unsteady Development of a Turbulent Wake Through a Downstream Low-Pressure Turbine Blade Passage," ASME J. Turbomach., **127**( 2), pp. 388–394.
[5] Wu, X., Jacobs, R. G., Hunt, J. C. R., and Durbin, P. A., 1999, "Simulation of Boundary Layer Transition Induced by Periodically Passing Wakes," J. Fluid. Mech., **398**, pp. 109–153.
[6] Wissink, J. G., Rodi, W., and Hodson, H. P., 2006, "The Influence of Disturbances Carried by Periodically Incoming Wakes on the Separating Flow Around a Turbine Blade," Int. J. Heat and Fluid Flow, **27**(4), pp. 721–729.
[7] Coull, J. D., and Hodson, H. P., 2011, "Unsteady Boundary-Layer Transition in Low-Pressure Turbines," J. Fluid. Mech., **681**, pp. 370–410.
[8] Opoka, M. M., and Hodson, H. P., 2008, "Experimental Investigation of Unsteady Transition Processes on High-Lift T106a Turbine Blades," J. Propul. Power., **24**(3), pp. 424–432.

[9] Lardeau, S., Leschzinerl, M., and Zaki, T., 2012, "Large Eddy Simulation of Transitional Separated Flow Over a Flat Plate and a Compressor Blade," Flow Turbul. Combust., **88**( 1–2), p. 19.
[10] McAuliffe, B. R., and Yaras, M. I., 2010, "Transition Mechanisms in Separation Bubbles Under Low- and Elevated-freestream Turbulence," ASME J. Turbomach., **132**(1), pp. 536–543.
[11] Lengani, D., and Simoni, D., 2015, "Recognition of Coherent Structures in the Boundary Layer of a Low-Pressure-Turbine Blade for Different Free-stream Turbulence Intensity Levels," Int. J. Heat and Fluid Flow, **54**, pp. 1–13.
[12] Đurovic, K., De Vincentiis, L., Pralits, J. O., Henningson, D. S., and Hanifi, A., 2021, "Free-Stream Turbulence Induced Boundary-Layer Transition in Low-Pressure Turbines," ASME J. Turbomach., **143**(8), p. 081015.
[13] Jacobs, R. G., and Durbin, P. A., 2001, "Simulations of Bypass Transition," J. Fluid. Mech., **428**, pp. 185–212.
[14] Andersson, P., Berggren, M. B., and Henningson, D. S., 1999, "Optimal Disturbances and Bypass Transition in Boundary Layers," Phys. Fluid., **11**, pp. 134–150.
[15] Luchini, P., 2000, "Reynolds-Number Independent Instability of the Boundary Layer Over a Flat Surface," J. Fluid. Mech., **404**, pp. 289–309.
[16] Matsubara, M., and Alfredsson, P. H., 2001, "Disturbance Growth in Boundary Layers Subjected to Free-Stream Turbulence," J. Fluid. Mech., **430**, pp. 149–168.
[17] Mans, J., de Lange, H. C., and van Steenhoven, A. A., 2007, "Sinuous Breakdown in a Flat Plate Boundary Layer Exposed to Free-Stream Turbulence," Phys. Fluid., **19**, p. 088101–1/4.
[18] Schlatter, P., Brandt, L., de Lange, H. C., and Henningson, D. S., 2008, "On Streak Breakdown in Bypass Transition," Phys. Fluid., **20**(10), p. 101505.
[19] Lengani, D., Simoni, D., Ubaldi, M., Zunino, P., and Bertini, F., 2017, "Coherent Structures Formation During Wake-Boundary Layer Interaction on a P Turbine Blade," Flow Turbul. Combust., **98**( 1), pp. 57–81.
[20] Rao, V., Tucker, P., Jefferson-Loveday, R., and Coull, J., 2013, "Large Eddy Simulations in Low-Pressure Turbines: Effect of Wakes at Elevated Free-Stream Turbulence," Int. J. Heat Fluid Flow, **43**, pp. 85–95.
[21] Michelassi, V., Chen, L., Pichler, R., Sandberg, R., and Bhaskaran, R., 2016, "High-Fidelity Simulations of Low-Pressure Turbines: Effect of Flow Coefficient and Reduced Frequency on Losses," ASME J. Turbomach., **138**(11), p. 111006.
[22] Lengani, D., Simoni, D., Ubaldi, M., Zunino, P., and Bertini, F., 2020, "Recognition of Structures Leading to Transition in a Low-Pressure Turbine Cascade: Effect of Reduced Frequency," ASME J. Turbomach., **142**(6), p. 061007.
[23] Schlatter, P., Stolz, S., and Kleiser, L., 2006, "Large-Eddy Simulation of Spatial Transition in Plane Channel Flow," J. Turbul., **7**, p. N33.
[24] Negi, P., Vinuesa, R., Hanifi, A., Schlatter, P., and Henningson, D., 2018, "Unsteady Aerodynamic Effects in Small-Amplitude Pitch Oscillations of an Airfoil," Int. J. Heat Fluid Flow, **71**, pp. 378–391.
[25] Negi, P. S., 2019, "Stability and Transition in Pitching Wings". Ph.D. thesis, Royal Institute of Technology (KTH), Stockholm, Sweden, November.
[26] Patera, A. T., 1984, "A Spectral Element Method for Fluid Dynamics: Laminar Flow in a Channel Expansion," J. Comput. Phys., **54**(3), pp. 468–488.
[27] Fischer, P. F., Lottes, J. W., and Kerkemeier, S. G., 2008, Nek5000 Web page. http://nek5000.mcs.anl.gov.
[28] Maday, Y., Mavriplis, C., and Patera, A. T., 1988, "Nonconforming Mortar Element Methods: Application to Spectral Discretizations," In Proceedings of the 2nd International Conference on Domain Decomposition Methods, pp. 392–418.
[29] Merrill, B. E., Peet, Y. T., Fischer, P. F., and Lottes, J. W., 2016, "A Spectrally Accurate Method for Overlapping Grid Solution of Incompressible Navier–Stokes Equations," J. Comput. Phys., **307**, pp. 60–93.
[30] Merrill, B. E., and Peet, Y. T., 2017, "Effect of Impinging Wake Turbulence on the Dynamic Stall of a Pitching Airfoil," AIAA. J., **55**(12), pp. 4094–4112.
[31] Peet, Y. T., and Fischer, P. F., 2012, "Stability Analysis of Interface Temporal Discretization in Grid Overlapping Methods," SIAM J. Numer. Anal., **50**(6), pp. 3375–3401.
[32] Schlatter, P., 2001, "Direct Numerical Simulation of Laminar-Turbulent Transition in Boundary Layer Subject to Free-Stream Turbulence". Diploma thesis, Royal Institute of Technology (KTH), Stockholm, Sweden.
[33] Berrino, M., Lengani, D., Simoni, D., Ubaldi, M., Zunino, P., and Bertini, F., 2015, "Dynamics and Turbulence Characteristics of Wake-Boundary Layer Interaction in a Low Pressure Turbine Blade," In Turbo Expo: Power for Land, Sea, and Air, American Society of Mechanical Engineers, Paper No. GT2015-42626.
[34] Hussain, A. K. M. F., and Reynolds, W. C., 1970, "The Mechanics of an Organized Wave in Turbulent Shear Flow," J. Fluid. Mech., **41**(2), pp. 241–258.